Research Square

Preprints are preliminary reports that have not undergone peer review.
They should not be considered conclusive, used to inform clinical practice,
or referenced by the media as validated information.

Synergistic Catalysis Enables Chemoselective Asymmetric Carbene N–H Insertion of Functionalized Anilines

Tetsuhiro Nemoto

tnemoto@faculty.chiba-u.jp

Chiba University https://orcid.org/0000-0001-8858-161X

Shingo Harada

Chiba univ. https://orcid.org/0000-0002-8373-4143

Tasuki Sakai

Chiba University

Maika Furutani

Chiba University

Article

Keywords:

Posted Date: July 2nd, 2026

DOI: https://doi.org/10.21203/rs.3.rs-10082654/v1

License: This work is licensed under a Creative Commons Attribution 4.0 International License.
Read Full License

Additional Declarations: There is **NO** Competing Interest.

Synergistic Catalysis Enables Chemoselective Asymmetric Carbene N–H Insertion of Functionalized Anilines

Shingo Harada,[*,1] Tasuki Sakai,[1,2] Maika Furutani,[1,2] and Tetsuhiro Nemoto[*,1]

[1]Graduate School of Pharmaceutical Sciences, Chiba University, 1-8-1, Inohana, Chuo-ku, Chiba 260-8675, Japan

[2]These authors contributed equally: Maika Furutani, Tasuki Sakai. e-mail: Sharada@chiba-u.jp; tnemoto@faculty.chiba-u.jp

Selective carbene transfer in the presence of multiple reactive functional groups represents a central objective in catalytic asymmetric synthesis. Chemoselective asymmetric N–H insertion in the presence of free alcohols has remained a formidable challenge in carbene chemistry because hydroxy functionalities can participate in competing pathways, perturb catalyst speciation, and disrupt the stereocontrolling proton-transfer manifold. Here, we disclose a catalytic asymmetric N–H insertion of anilines bearing unprotected alcohol functionalities that proceeds with high enantioselectivity and chemoselectivity. Enabled by synergistic catalysis between ruthenium(II) and a chiral N,O-bifunctional organocatalyst, this transformation provides efficient access to *N*-aryl α-amino ester derivatives in high yields. Although enantioselective photochemical carbene-transfer reactions remain underdeveloped, we further establish a complementary blue-light-driven protocol using the same organocatalyst, which is effective for selected substrates that are less compatible with metal-catalyzed conditions.

Carbenes—highly reactive, formally divalent carbon species—have long stood as cornerstones of the chemical sciences[1,2,3]. Valued for their exceptional synthetic versatility[4,5,6,7], these species are predominantly accessed from diazo precursors through thermal, photochemical, transition-metal-catalyzed, or Lewis acid-mediated activation (Fig. 1a)[8,9,10,11,12]. Their rich chemistry underpins a broad spectrum of transformations, among which insertion reactions are synthetically distinctive[13,14,15,16,17]. N–H insertion, in particular, offers a direct and efficient route to functionalized amines and α-amino acid equivalents[18,19]. Enantioselective N–H insertion reactions have evolved along with the continued development of asymmetric catalysis, enabling the use of aliphatic amines[20], amides[21,22], anilines[23,24,25], carbamates[26], hydrazones[27], carbazoles[28], and imines.[29] Pioneering contributions by Doyle[27], Van Vranken[28], Bi[18], Zhu[13,20], Zhou[20,21,22], and other leading researchers have established distinct chiral catalytic platforms that deliver high enantiocontrol[30,31,32].

As part of our ongoing efforts to advance carbene chemistry[33,34], we recently reported a silver–rhodium dual catalytic platform for N–H insertion of heteroaromatics[35]. Despite these advances, simultaneously achieving high enantioselectivity, high yield, and broad functional-group compatibility remains challenging in representative N–H insertion reactions involving anilines[23,24,25]. In particular, reactions of donor/acceptor carbenes with anilines represent synthetically valuable yet mechanistically complex transformations for which a detailed understanding remains limited. Such reactions provide direct and efficient access to a diverse range of biologically and medicinally relevant compounds, including isotopically labelled nucleic acids, as well as DNA/RNA alkylation products with broad applicability (Fig. 1c)[36].

Recent efforts have focused on expanding the generality of N–H insertion reactions, particularly for substrates bearing unprotected hydroxy functionalities[37]. In this context, Wang, Li, Toste, Zhao, and co-workers developed elegant strategies for controlling chemoselectivity using single-atom Rh catalysts (Fig. 1d)[38]. Similarly, Zhao and Niu achieved chemoselective N–H insertion over competing O–H insertion using Cu nanowire (NW) catalysts[39]. To the best of our knowledge, however, no catalytic system has yet achieved simultaneous control of chemoselectivity and enantioselectivity in the N–H insertion of substrates bearing unprotected hydroxy functionalities.

Whereas chiral phosphoric acids and thiourea variants[20,21,35,40,41] are predominant chiral sources in enantioselective X–H insertion, the present study reveals that a novel chiral tertiary amine derivative can function as an effective chiral inducer. In general, Lewis basic species pose significant compatibility challenges due to their propensity to coordinate with the metal center, thereby inhibiting catalytic activity (Fig. 1b). In 2019, Zhou, Zhu, and coworkers reported a landmark N–H insertion of basic amines, enabled by an ingeniously designed catalysis comprising a chiral thiourea and Tp*Cu that effectively suppresses undesired amine–metal complexation[20]. In contrast, the present investigation revealed that N–H insertion can be achieved through cooperative catalysis[42,43,44] between a readily available ruthenium catalyst[45,46] and a basic organocatalyst. Mechanistic investigations further revealed that enantioselectivity is governed by asymmetric protonation following metal-associated ylide formation. These studies suggested that, although photochemical carbene reactions of diazo compounds traditionally afford racemic products, asymmetric induction might be achievable under photochemical conditions through a related

mechanistic pathway[47]. A potential concern, however, is that the amine nucleophile itself may function as a proton shuttle in place of the chiral amine catalyst, thereby undermining asymmetric induction (Fig. 1b)[18,48]. Systematic investigation ultimately enabled control of enantioselectivity under photochemical conditions, with the reaction showing functional-group compatibility complementary to that of metal catalysis. During these investigations, we observed an intriguing phenomenon wherein lowering the reaction temperature improved the yield but diminished the enantioselectivity. Although anomalous temperature-dependent changes in enantioselectivity are documented in the literature[49], the mechanistic factors governing such behavior are often complex and highly system-specific. Combined computational and experimental studies indicate that the phenomenon arises from a proton-shuttle mechanism mediated by a hydrogen-bonding network assembled from multiple anilines, the formation of which is favored at lower temperatures owing to a reduced entropic penalty.

Here, we describe complementary enantioselective aniline N–H insertion enabled by ruthenium catalysis and blue-light irradiation, along with detailed mechanistic studies.

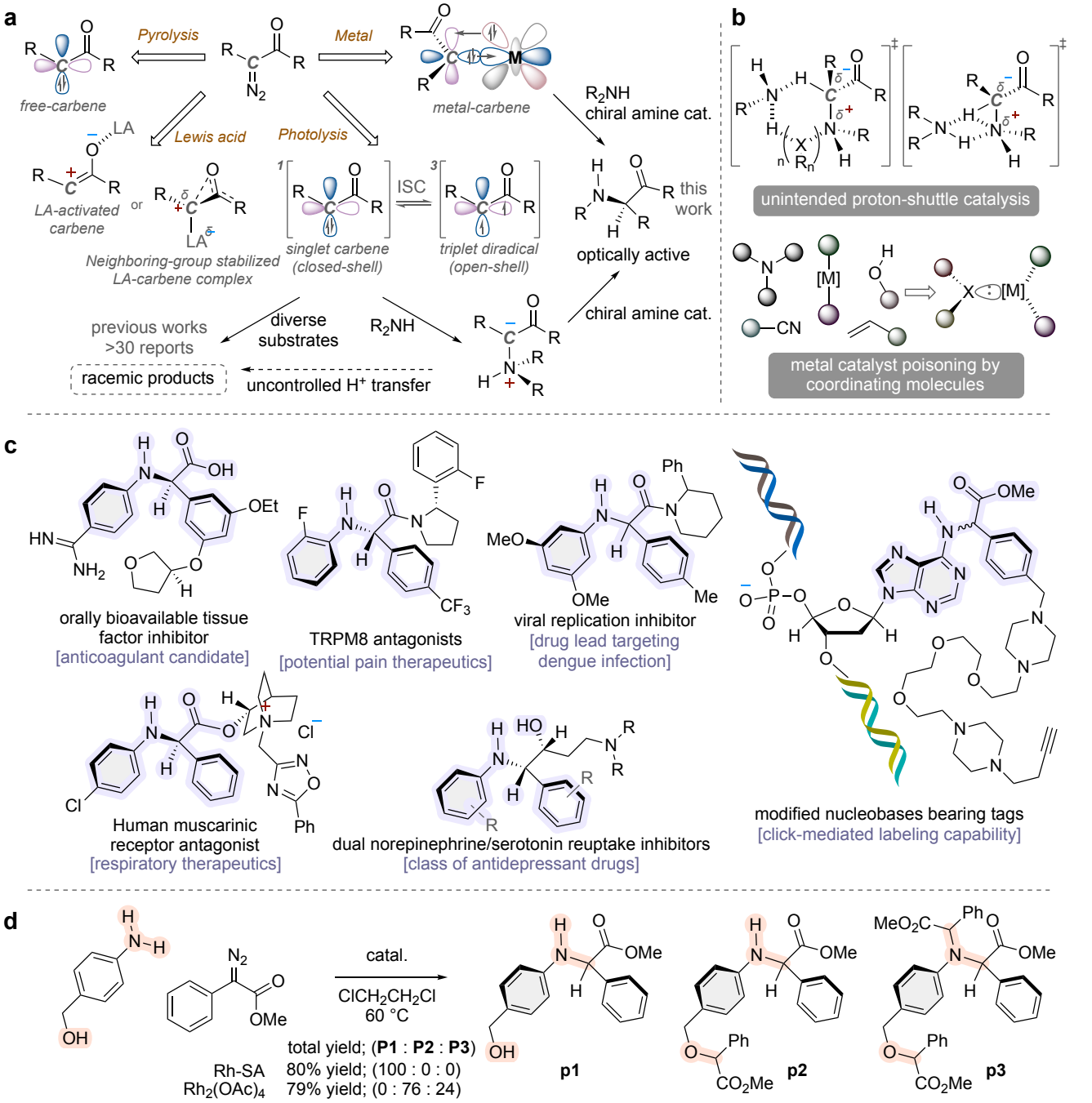
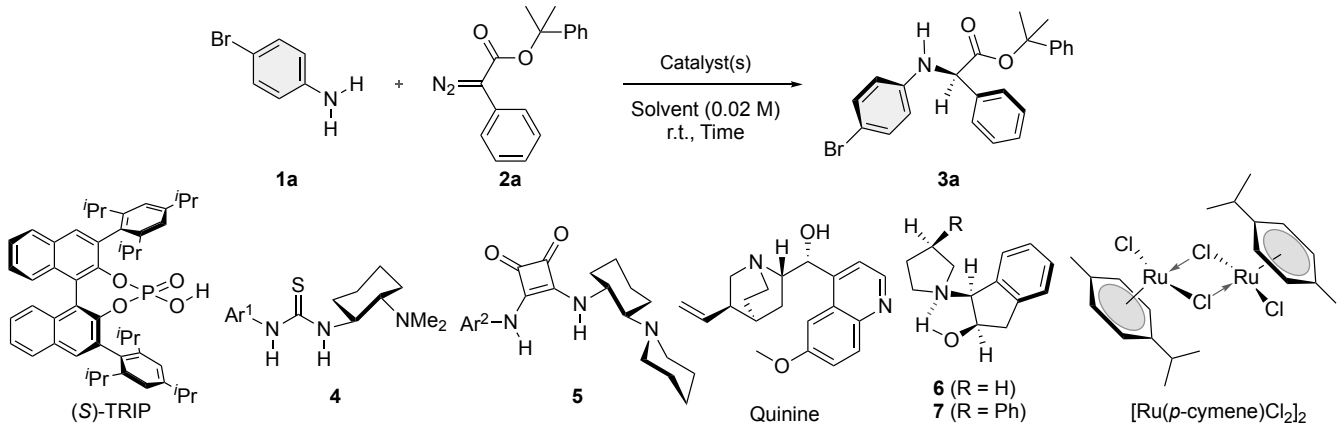


Fig. 1 | Background and design concept of the present study. a, Distinct modes of carbene generation and divergent reactivity. **b**, Inherent challenges in asymmetric carbene insertion into N–H bonds. **c**, Bioactive molecules bearing aniline-derived α-amino acid scaffolds and related variants. **d**, Pioneering example of chemoselective N–H insertion over O–H insertion affording racemic products.

Results

Identification and optimization of the cooperative catalysis. We began our investigation using aniline derivative **1a** and donor/acceptor-substituted diazo compound **2a** to identify optimal conditions for the enantioselective N–H insertion reaction (Table 1). Chiral rhodium(II) catalysis at ambient temperature in toluene afforded the desired product **3a** in 69% yield with an enantiomeric ratio (e.r.) of 58:42 (entry 1). Relay catalysis combining rhodium with a chiral phosphoric acid modestly improved the enantioselectivity (entry 2). Although chiral thiourea, squaramide, and quinine proved ineffective (entries 3–5), further screening revealed that chiral tricyclic organocatalyst **6** afforded **3a** in 90:10 e.r. (entry 6). Subsequent evaluation of catalyst parameters in combination with **6** identified the ruthenium-based system as uniquely effective (entries 7–14). Varying the ligand on the ruthenium catalyst was unproductive (entries 15 and 16); however, subsequent solvent screening identified dichloromethane as the optimal medium (94:6 e.r., entry 17, Supplementary Table 1). Fine-tuning of the catalyst structure and loading ultimately established entry 19 as optimal (entries 18 and 19).

Table 1 | Catalyst evaluation[a]



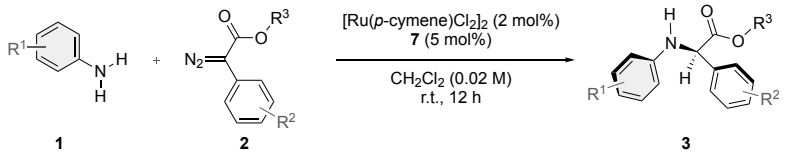
Entry	Catalyst(s) (mol%)	Solvent	Time (h)	Yield (%)	e.r.
1	Rh_2((*R*)-PTTL)$_4$	toluene	24	69	58:42
2	$Rh_2(OAc)_4$ (2) & (*S*)-TRIP (2)	toluene	5	55	71:29
3	$Rh_2(OAc)_4$ (2) & **4** (2)	toluene	5	71	58:42
4	$Rh_2(OAc)_4$ (2) & **5** (2)	toluene	5	70	13:87
5	$Rh_2(OAc)_4$ (2) & Quinine (2)	toluene	5	80	45:55
6	$Rh_2(OAc)_4$ (2) & **6** (2)	toluene	5	76	90:10
7	$Rh_2(OCOCPh_3)_4$ (2) & **6** (2)	toluene	24	9	82:18
8	[Cp*Rh(MeCN)$_3$][SbF_6]$_2$ & **6** (2)	toluene	5	52	51:49
9	Cp_2HfCl_2 (2) & **6** (2)	toluene	5	0	-
10	$Pd_2(dba)_3$ (2) & **6** (2)	toluene	24	55	64:36
11	[Ru(*p*-cymene)I_2]$_2$ (2) & **6** (2)	toluene	5	92	88:12
12	[Ru(*p*-cymene)Cl_2]$_2$ (2) & **6** (2)	toluene	5	90	91:9
13	[Ru(*p*-cymene)Cl_2]$_2$ (2), $AgNTf_2$ (2) & **6** (2)	toluene	19	60	51:49
14	[Ru(*p*-cymene)Cl_2]$_2$ (2), $AgOCOCF_3$ (2) & **6** (2)	toluene	24	16	56:44
15	$RuCl_2$[(*R*)-xylbinap][(*R*)-daipen] (2) & **6** (2)	toluene	24	0	-
16	Cp*RuCl(PPh_3)$_2$ (2) & **6** (2)	toluene	24	15	79:21
17	[Ru(*p*-cymene)Cl_2]$_2$ (2) & **6** (2)	CH_2Cl_2	5	91	94:6
18	[Ru(*p*-cymene)Cl_2]$_2$ (2) & **7** (2)	CH_2Cl_2	5	82	95:5
19	[Ru(*p*-cymene)Cl_2]$_2$ (2) & **7** (5)	CH_2Cl_2	12	95	97:3

[a] Reaction conditions: catalyst (indicated mol%), **1a** (0.6 mmol), **2a** (0.2 mmol) in CH_2Cl_2 (10.0 mL) at room temperature unless otherwise noted. e.r., enantiomeric ratio. Rh_2((*R*)-PTTL)$_4$, dirhodium tetrakis[*N*-phthaloyl-(*R*)-*tert*-leucinate]. daipen, 1,1-bis(4-methoxyphenyl)-3-methyl-1,2-butanediamine. Cp*, pentamethylcyclopentadienyl.

Scope and limitations of the Ru/organocatalyst system. We next explored the substrate generality (Fig. 2). Anilines bearing electron-withdrawing substituents—including fluoro, trifluoromethyl, ester, methyl ketone, and nitro groups—reacted smoothly to afford the corresponding products in good yields with high enantioselectivities, underscoring the broad functional group tolerance (**3b**–**g**, 61–95% yield, 94:6–97:3 e.r.). Substrates bearing nitrile groups capable of coordinating to the ruthenium center, however, exhibited

diminished enantioselectivity (**3h**, 76:24 e.r.). In addition to unsubstituted aniline (**3i**), substrates bearing substituents at the meta or ortho positions, as well as electron-donating groups, were well tolerated (**3j**-**m**). Importantly, the present protocol accommodated a monosubstituted terminal alkene (**3n**, 93:7 e.r.), despite its propensity for undesired cyclopropanation in Rh(II)-mediated carbene transfer[38]. The reaction of naphthylamine also proved feasible; however, introduction of a naphthyl group at the α-position of the diazo counterpart diminished the enantioselectivity (**3o** and **3p**, 95:5 and 76:24 e.r., respectively).

The carbene precursor exhibited broad electronic tolerance at the aryl position, accommodating both electron-withdrawing and electron-donating substituents (**3q**–**w**, 92:8–97:3 e.r.). The *tert*-butyl ester variant furnished crystals suitable for X-ray diffraction analysis, enabling assignment of absolute configuration (**3x**). Benzocaine, a widely used local anesthetic, was also well tolerated in the asymmetric N–H insertion protocol, furnishing the desired product **3y** in 95% yield and 97:3 e.r. Despite their attenuated nucleophilicity, 2-aminobenzophenone, a key precursor to central nervous system-depressant benzodiazepines, and aminotetralone derivatives were also compatible (**3z**–**3ab**). Increasing the catalyst loading in the reaction with aminopyrene afforded the corresponding chiral fluorescent dye **3ac**. Additionally, dapsone, a drug used to treat leprosy, underwent twofold N–H insertion, affording **3ad** as a single enantiomer with excellent stereoselectivity (93:7 dr, 99:1 e.r.).



1 2 3

3b 84% yield, 95 :5 er

3c 61% yield, 94 : 6 er

3d 95% yield, 96 : 4 er

3e 95% yield, 96 : 4 er

3f 94% yield, 97 : 3 er

3g 75% yield, 96 : 4 er

3h 84% yield, 76 : 24 er

3i 77% yield, 97 : 3 er

3j 76% yield, 97 : 3 er

3k[a] 71% yield, 93 : 7 er

3l[a] 97% yield, 92 : 8 er

3m 95% yield, 96 : 4 er

3n 68% yield, 93 : 7 er

3o 89% yield, 95 : 5 er

3p quant., 76 : 24 er

3q 95% yield, 95 : 5 er

3r 60% yield, 94 : 6 er

3s 75% yield, 95 : 5 er

3t 97% yield, 92 : 8 er

3u 75% yield, 95 : 5 er

3v 89% yield, 96 : 4 er

3w 77% yield, 97 : 3 er

3x 58% yield, 95 : 5 er

X-ray of **3x**

CCDC No. 2556663

3y 95% yield, 97 : 3 er from Benzocaine

3z quant., 84 : 16 er for Benzodiazepines

3aa[a] 88% yield, 90 : 10 er

3ab 95% yield, 86 : 14 er

3ac[a] 79% yield, 94 : 6 er for fluorescence probing

3ad[b] 86% yield, 93 : 7 dr, 99 : 1 er from Dapsone

Fig. 2 | Scope of Ru-catalyzed carbene transfer reactions. [a] $[Ru(p\text{-cymene})Cl_2]_2$ (3.5 mol%) and **7** (7 mol%) were used. [b] Diazo compound and aniline source were used in a 2:1 ratio.

Mechanistic investigation of the Ru-catalyzed asymmetric N–H insertion. We turned our attention to mechanistic aspects of the Ru/amine catalysis. A labelling experiment using deuterated aniline furnished the corresponding product bearing deuterium exclusively at the ester α-position (Supplementary Fig. 1). Mechanistic insights into the observed synergism were obtained through quantum chemical investigations[50,51]. The calculated reaction coordinate for the N–H insertion reaction, modeled with a simplified catalyst structure, is presented in Fig. 3a (Supplementary Table 6). The C–N bond-forming step is initiated by engagement of the electrophilic Ru–carbene species with the aniline nitrogen, proceeding with an activation barrier of only 2.66 kcal mol^{-1}[52]. The resulting Ru-associated ammonium ylide **CP2**$_{Assoc}$ is further stabilized by a pair of N–H···Cl hydrogen bonds (2.02 and 2.21 Å). The energetically unfavorable dissociation of the Ru catalyst underscores the importance of the Ru dihalide complex in maintaining catalyst association throughout the reaction pathway (**INT1**$_{DISS}$, +20.87 kcal mol^{-1}). The organocatalyst subsequently mediates proton abstraction from the anilinium moiety via **TS2**, affording **CP4** with an activation barrier of +4.39 kcal mol^{-1} relative to **CP3**. The N–H insertion reaction is completed by protonation of the more reactive *O*-bound Ru enolate **CP5**, generated through C-to-O linkage isomerization of **CP4** (Ru···C = 2.37, Ru···O = 2.17 Å), by an ammonium-activated hydroxy functionality.

We next systematically investigated the enantiodetermining proton-transfer processes. To provide a rational basis for the superior performance of the optimized catalytic system, the steric environment around the catalytic pocket was visualized using topographic steric maps (Fig. 3b)[53]. Centered on the oxygen atom acting as the proton donor, the Ru–enolate complex associated with **7** exhibited an asymmetric steric environment, characterized by heavily occupied southwest and northeast quadrants ($\%V_{bur}$(SW) = 71.0, $\%V_{bur}$(NE) = 76.1, **7-Ru**$_{enolate}$). In contrast, the **Quinine-Ru**$_{enolate}$ complex displayed minimal quadrant-dependent variation in %Vbur, indicating a poorly differentiated chiral environment. By comparison, the chiral phosphoric acid catalyst, a privileged catalyst class for asymmetric N–H insertion, was extensively embedded within the surrounding steric volume (**(*S*)-TRIP-Ru**$_{enolate}$), suggesting a distinct alternative mechanistic manifold.

To elucidate the origin of enantioinduction, we compared the competing transition states leading to the *R*- and *S*-configured products (Fig. 3c). In both located saddle-point structures, the enolate, the piano-stool Ru complex, and the onium species were closely associated within a well-organized ternary assembly. The energetically favored pathway proceeding through **TS3**$_{major}$ has an activation barrier of +14.36 kcal mol^{-1}, whereas **TS3**$_{minor}$, arising from Re-face approach of the onium species, requires a higher barrier of +16.45 kcal mol^{-1}. The corresponding C–H-forming and O–H-breaking distances (**TS3**$_{major}$: 1.32/1.31 Å; **TS3**$_{minor}$: 1.33/1.29 Å) suggest that **TS3**$_{minor}$ has a marginally earlier transition state. Nevertheless, conformational analysis alone did not reveal a dominant stereochemical determinant.

To elucidate the energetic origins of the observed selectivity, we performed an activation strain analysis[54] with BSSE correction using the counterpoise method. Notably, **TS3**$_{major}$ exhibited a larger total strain energy than **TS3**$_{minor}$ by 3.03 kcal mol^{-1}, with values of 65.01 and 61.98 kcal mol^{-1}, respectively. This destabilizing contribution, however, was more than offset by a more favorable interaction energy (5.27 kcal mol^{-1}), ultimately rendering **TS3**$_{major}$ energetically preferred. We, thus, further analyzed the interactions among these reaction components by NCI plotting (Fig. 3d). Within **nci-TS3**$_{major}$, in addition to the conventional onium N^+–H···Cl hydrogen bond, nonclassical C–H···Cl interactions from the aminomethylene $C(sp^3)$–H bonds and the aryl $C(sp^2)$–H bonds of the pyrrolidine-based catalyst framework were also identified. These cooperative interactions help organize the formal eight-membered ruthenacyclic transition state in a manner reminiscent of outer-sphere ligand effects. Although **nci-TS3**$_{minor}$ likewise exhibited a diverse set of weak attractive interactions, including C–H···π contacts, **nci-TS3**$_{major}$ displayed more extensive London-dispersion-dominated forces. Taken together, these theoretical insights are consistent with the observed enantioselectivity and provide a compelling mechanistic rationale for the synergy of this unique catalyst combination.

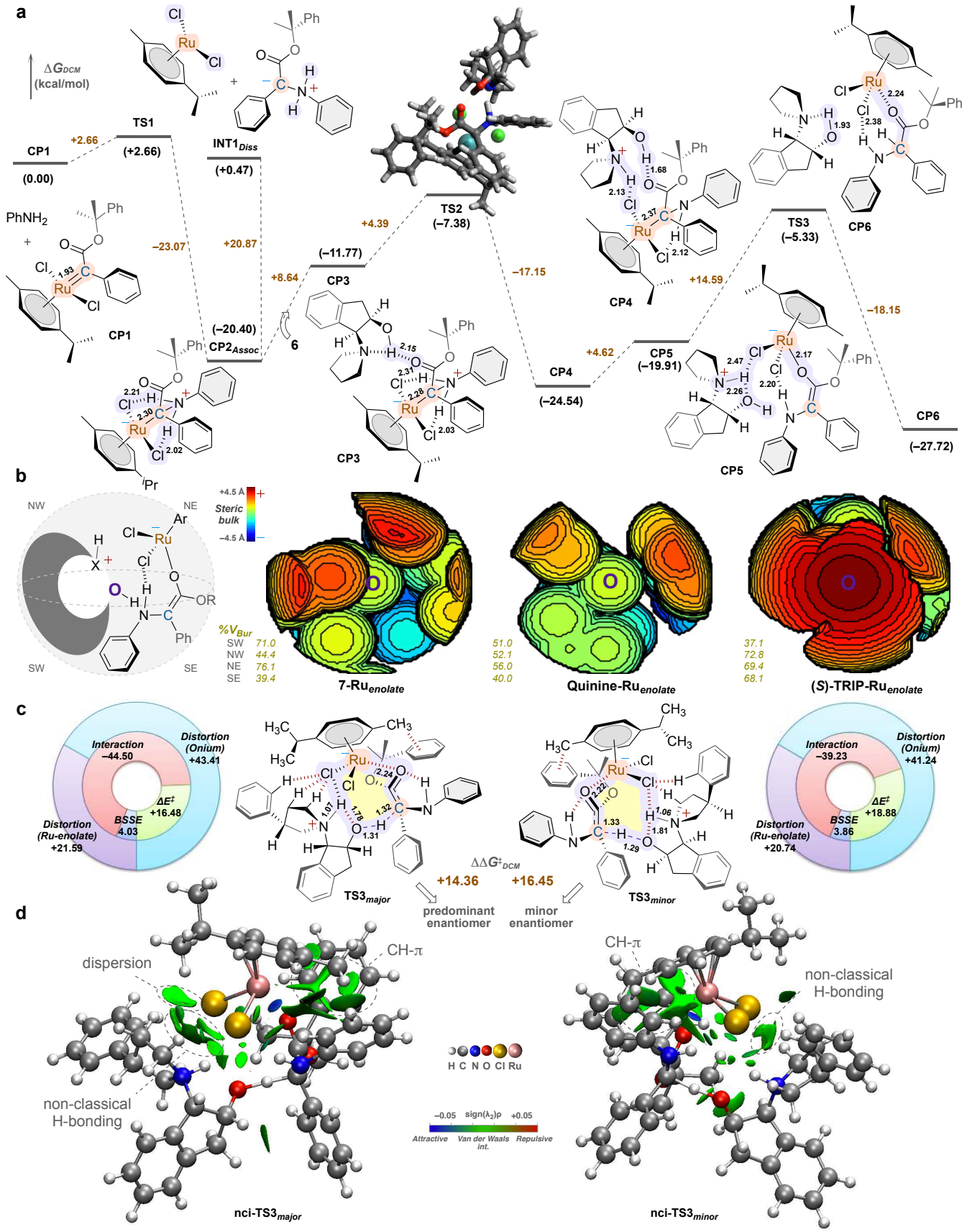


Fig. 3 | Mechanistic investigations of Ru/organocatalyst cooperative catalysis. a, Reaction coordinate diagram. Computation was implemented at the rM08-HX/SDD(Ru)/6-311++G**//rb3lyp/def2-SVPP levels of theory in CH_2Cl_2 solvent. Selected distances are given in Å. **b**, Topographic steric maps generated using SambVca 2.1 with a sphere radius of 4.5 Å. **c**, Distortion/interaction (activation-strain) analysis of transition states with BSSE corrections applied to account for basis set superposition error. **d**, Noncovalent interaction (NCI) plots visualized with VMD, mapping weak interaction regions based on electron density (ρ) and the reduced density gradient (RDG).

Chemoselective N–H insertion in the presence of free alcohols. To further expand the catalytic scope, we next examined anilines bearing unprotected hydroxy groups, a substrate class for which simultaneous control of chemoselectivity and enantioselectivity remains unprecedented (Fig. 1d). When (4-aminophenyl)methanol **8a** was subjected to the ruthenium-catalyzed conditions, chemoselective N–H insertion proceeded efficiently to deliver the corresponding secondary amine **9a** in quantitative yield and 93:7 e.r. (Fig. 4a). In contrast, alternative systems based on transition-metal catalysis, Lewis acid catalysis, or thermal activation were less effective. The robustness of chemoselective N–H insertion over O–H insertion was further demonstrated through substrate-scope studies (Fig. 4b). Electronically diverse ruthenium-carbene species afforded the products in good to quantitative yields with high enantioselectivities. (**9b**–**i**, 57% to quant., 87:13 to 95:5 e.r.). Aminophenyl ethanol derivatives were likewise converted into the desired products **9j** and **9k**. Additional amine sources, including *p*-amino-*m*-fluorobenzyl alcohol and *p*-amino-*o*-methylbenzyl alcohol, were also well tolerated (**9n** and **9m**, quant. and 71% yield, 95:5 and 96:4 e.r., respectively).

To gain insight into the origin of the observed chemoselectivity, quantum chemical calculations were conducted. As depicted in Fig. 3a, formation of the Ru-associated ylide is not rate-limiting; instead, the following step proceeds irreversibly, thereby governing the observed chemoselectivity. We therefore identified the transition states for *O*- and *N*-ylide formation (Fig. 4c). Formation of the Ru-associated *N*-ylide (**Ru-N$_{ylide}$**) was calculated to be kinetically favored by 7.17 kcal mol^{-1} over formation of the corresponding *O*-ylide ($\Delta G^{\ddagger}$ = +2.01 vs +9.18 kcal mol^{-1}). This pronounced energetic bias provides a clear rationale for the absence of detectable *O*-ylide formation across the examined substrate scope.

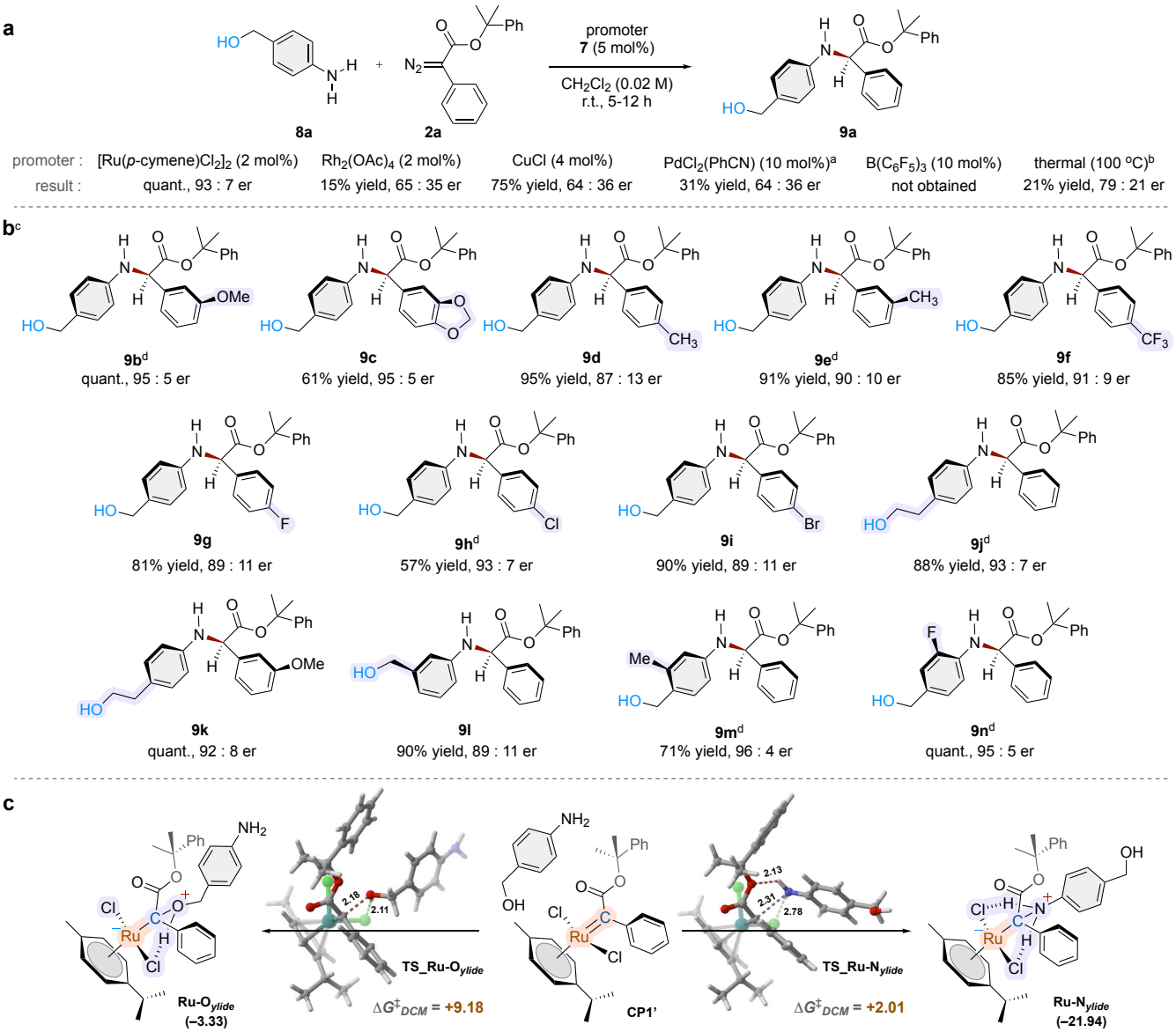


Fig. 4 | Asymmetric N–H insertion of anilines bearing unprotected hydroxy groups. a, Evaluation of catalytic performance. **b**, Enantioenriched *N*-alkylated products. **c**, Comparative analysis of the N–H and O–H insertion pathways and activation barriers. [a] $NaBArF_4$ (10 mol%) was used. [b] The reaction was performed in toluene for 12 h. [c] Unless otherwise noted, $[Ru(p\text{-cymene})Cl_2]_2$ (3.5 mol%) and **7** (7 mol%) were used. [d] $[Ru(p\text{-cymene})Cl_2]_2$ (2 mol%) and **7** (5 mol%) were used.

A metal-free asymmetric N–H insertion enabled by blue light. Next, we turned our attention to the enantioselective photochemical reaction[55]. As shown in Fig. 1a, photoinduced carbene generation produces singlet or triplet free carbenes, resulting in predominantly racemic outcomes. Nevertheless, we reasoned that, in X–H insertion reactions, enantioselectivity can be established during the protonation step following ylide formation between a free carbene and the heteroatom, rendering asymmetric induction feasible in principle.

After optimization (Supplementary Tables 3–5), blue-light irradiation of **1a**, **2a**, and **7** in toluene afforded **3a** in 55% yield with 95:5 e.r. (entry 1, Fig. 5a). The high reactivity of the free carbene, however, rendered precise stereochemical control challenging, limiting the yield to a moderate level. Although lowering the reaction temperature improved the yield, counterintuitively, it was accompanied by a notable decrease in enantioselectivity (entries 2–5). Increasing the amount of aniline from 3 to 10 equivalents improved the yield but similarly led to diminished enantioselectivity at lower temperatures (entries 6–10). The decrease was more pronounced at higher aniline loadings, suggesting the involvement of additional aniline molecules in the enantiodetermining step under low-temperature conditions (entry 1 vs 5 and entry 6 vs 10; 90 to 54% ee and 90 to 42% ee, respectively). In contrast, the absence of a nonlinear effect suggests that enantiodetermination is governed by a single catalyst molecule.

Balancing yield and selectivity, the optimal reaction conditions were 2 mol% of catalyst and six equivalents of aniline at 4 °C for 12 h; these conditions were subsequently applied to a range of substrates (Fig. 5b). Notably, for sterically demanding substrates, such as naphthyl-substituted carbene precursors, the metal-free conditions occasionally outperformed the Ru-catalyzed system in terms of enantioselectivity (**3p**, 95:5 vs 76:24). Furthermore, substrates bearing a nitrile group capable of coordinating to the transition-metal catalyst exhibited marked differences in enantioselectivity under the two sets of conditions (**3h**, 91:9 vs 76:24). Together, these results demonstrate that visible-light irradiation can serve as a complementary promoter to metal catalysis in asymmetric N–H insertion reactions.

Mechanism of the visible-light-promoted N–H insertion process. To clarify the mechanism of the photochemical process, we conducted a series of mechanistic investigations (Fig. 5c). When deuterated aniline was used, deuterium was incorporated into the aminomethine carbon of the product (eq 1). Control experiments (eqs 2 and 3) ruled out any post-formation change in the enantiomeric purity of the product. Adding TEMPO markedly decreased the product yield to 23% (eq 4). Spectroscopic analysis showed that the absorption profile of **2a** remained unchanged upon addition of **7**, whereas an emission maximum was observed at around 500 nm. To gain further insight into the reaction pathway, time-dependent density functional theory (TD-DFT) calculations[56] were performed (Fig. 6a). The calculated S_0-to-singlet Franck–Condon excitation of the carbene precursor requires 60.03 kcal mol^{-1} (***S*$_n$-2a**), followed by vibrational relaxation and internal conversion (IC) of the S_n state to S_1, located +39.13 kcal mol^{-1}. Subsequent intersystem crossing to the triplet manifold occurs through spin–orbit coupling, enabling the otherwise spin-forbidden singlet–triplet transition and ultimately generating the triplet intermediate T_1 at 27.96 kcal mol^{-1}. Extrusion of N_2 from the **T$_1$-2a** proceeds with an activation barrier of 13.75 kcal mol^{-1} to afford triplet carbene (**^{3}Carbene**), whereas direct carbene generation from S_0 requires a substantially higher energy (>30 kcal mol^{-1}). The generated triplet species is converted to the corresponding singlet **^{1}Carbene** *via* intersystem crossing through the minimum energy crossing point (MECP) on the seam of crossing (SX) within the Marcus theory.[57] In the triplet state, the singly occupied molecular orbital (SOMO) of the carbene is conjugated with the adjacent carbonyl group, whereas in the singlet state, the corresponding orbital is vacant, resulting in a nearly orthogonal arrangement with a dihedral angle of 85.7°. The geometry at the MECP partakes of both limiting electronic configurations and can be described in terms of interacting frontier molecular orbitals (IFMOs). The resulting electrophilic singlet carbene is readily intercepted by the aniline nitrogen to form the C–N bond (+6.53 kcal mol^{-1}, **TS5**). The resulting dipolar intermediate **IN1** then collapses to the intramolecularly hydrogen-bonded enol **IN2** with essentially no additional barrier, rendering the sequence exergonic.

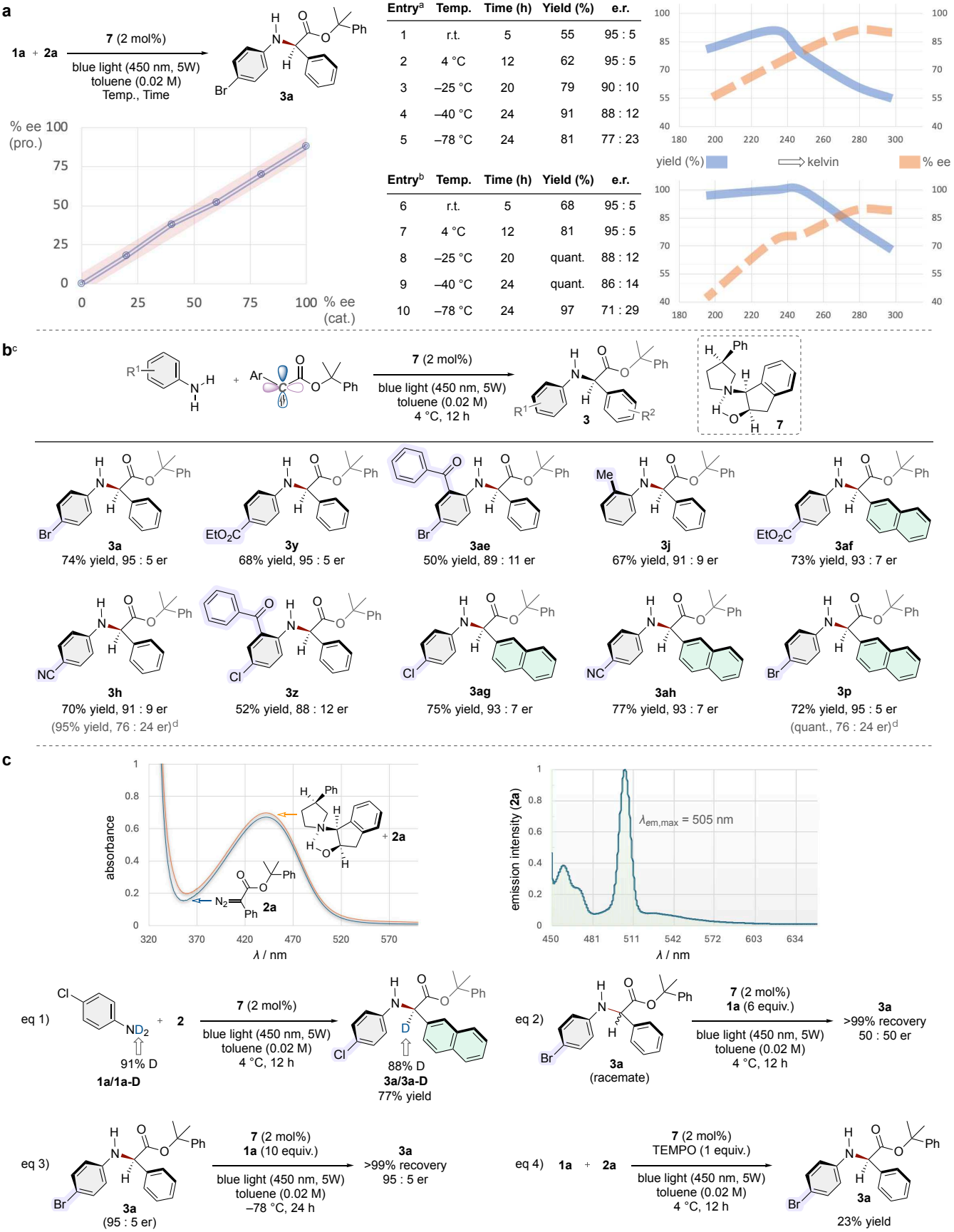


Fig. 5 | Photochemical organocatalysis. a, Temperature-dependent enantioselectivity. **b**, Enantioenriched products from blue-light-promoted N–H insertion reactions. **c**, Mechanistic insights. [a] Reaction conditions: **1a** (0.3 mmol), **2a** (0.1 mmol), **7** (0.002 mmol) in toluene (5.0 mL). [b] Reaction conditions: **1a** (1.0 mmol), **2a** (0.1 mmol), **7** (0.002 mmol) in toluene (5.0 mL). [c] Reaction conditions: **1** (1.2 mmol), **2** (0.2 mmol), **7** (0.004 mmol) in toluene (10.0 mL). [d] For comparison with the metal-catalyzed conditions: $[Ru(p\text{-cymene})Cl_2]_2$ (0.004 mmol), **1a** (0.6 mmol), **2a** (0.2 mmol), and **7** (0.01 mmol) in CH_2Cl_2 (10 mL).

Analysis of the enantiodetermining process from **IN2** revealed that the chiral amine orchestrates an efficient proton-transfer (Fig. 6b). In $\mathbf{TS7}_{major}$, interaction of the basic amine unit with the enolic O–H generates incipient ammonium character, rendering the intramolecular hydroxy group sufficiently acidic to serve as the proton donor. NCI analysis indicated a nonclassical hydrogen-bonding interaction between the cationic aminomethylene moiety of the organocatalyst and the aniline-derived nitrogen atom. In contrast, although $\mathbf{TS7}_{minor}$ also proceeds through an onium-assisted proton-transfer pathway, the aniline moiety is subject to competing attractive and repulsive interactions with the catalyst. At 298 K, the calculated Gibbs free energy difference between $\mathbf{TS7}_{major}$ and $\mathbf{TS7}_{minor}$ was 1.974 kcal mol^{-1}, corresponding to an estimated rate constant ratio of 96.5:3.5. At 195 K, however, this energy difference increased to 2.58 kcal mol^{-1}, which is incompatible with the experimentally observed erosion of enantioselectivity. Because the present blue-light-promoted reaction remains operative in the absence of the organocatalyst, we next considered the possible involvement of proton-shuttle catalysis.[18,48] The pathway mediated by a single additional aniline molecule (**TS8**), in which deprotonation of the enolic proton occurs concomitantly with α-protonation, exhibited an activation barrier of approximately 17.8 kcal mol^{-1} at both 298 and 195 K, indicating that this process is unlikely to be kinetically operative. Nevertheless, identification of saddle points corresponding to a multimolecular proton-shuttle pathway involving hydrogen-bonding molecular ensembles revealed pronounced temperature-dependent differences in activation energy. The magnitude of this effect increased with the number of participating molecules, concomitant with the emergence of increasingly extensive networks of noncovalent interactions. Specifically, the corresponding energy differences for **TS8**, **TS9**, **TS10**, and **TS11**, which are associated with racemic product formation, were 0.018, 1.08, 4.89, and 5.80 kcal mol^{-1}, respectively. Notably, **TS11** features a tetrameric aniline assembly stabilized by short hydrogen-bonding contacts of less than 2.1 Å among the four components, which lowers the activation barrier to 9.423 kcal mol^{-1} and renders this pathway highly competitive with $\mathbf{TS7}_{major}$ at 195 K (9.262 kcal mol^{-1}). When the Boltzmann-weighted contributions of all relevant pathways are considered together, the multimolecular proton-shuttle system provides a compelling rationalization for the experimentally observed modulation of enantioselectivity at low temperature. Formation of **TS11** requires multiple molecules to organize into a highly ordered transition-state assembly, substantially reducing the degrees of freedom in the system and imposing a marked entropic penalty. Because the entropic contribution to the Gibbs free energy scales with absolute temperature, the entropic penalty associated with these highly ordered multimolecular transition states becomes increasingly pronounced at higher temperatures, rendering their Boltzmann-weighted contributions to the overall enantioselectivity negligible under ambient conditions. Although the involvement of larger supramolecular ensembles comprising dozens of molecules cannot be entirely excluded, the present work establishes multimolecular transition states as a useful conceptual framework for rationalizing temperature-dependent changes in enantioselectivity.[49]

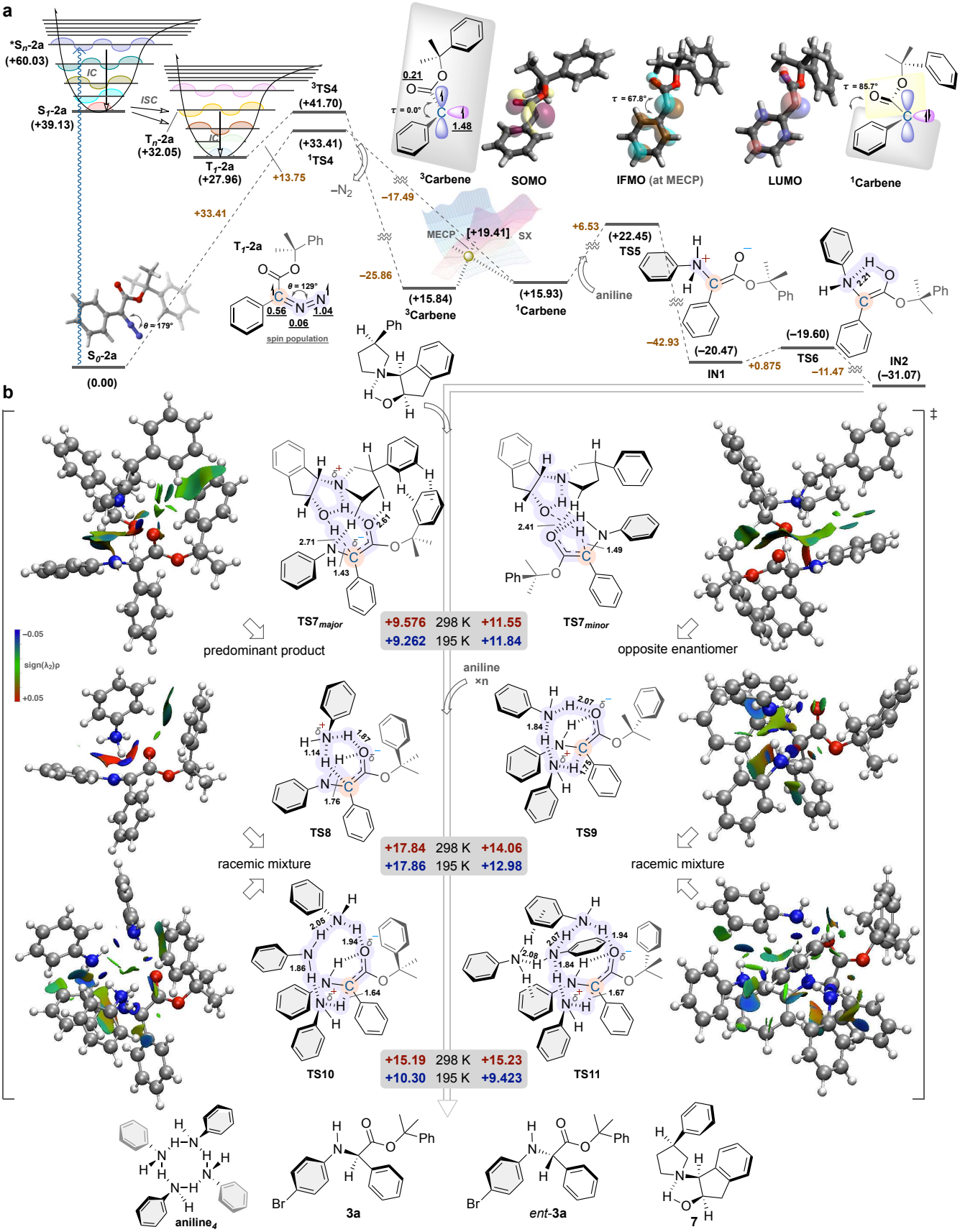


Fig. 6 | Mechanistic investigations of the metal-free photochemical organocatalytic cycle. a, Potential energy surface along the reaction pathway and visualization of key molecular orbitals. Computation was implemented at the (R/U)M08-HX/6-311++G**//(R/U)b3lyp/def2-SVPP levels of theory in toluene solvent, applying restricted and unrestricted formalisms for closed-shell and open-shell species, respectively. Distances are given in Å. **b**, Multicomponent protonation event and its temperature-dependent activation barrier.

Conclusions

In summary, we developed a synergistic catalytic platform for chemoselective asymmetric N–H insertion of anilines bearing unprotected alcohol functionalities. Although the ruthenium-carbene chemistry has been described as underdeveloped and limited by a narrow substrate scope[19], the cooperative combination of a ruthenium(II) complex and a chiral N,O-bifunctional catalyst—introduced here as a previously unexplored organocatalyst scaffold—enabled efficient access to *N*-aryl α-amino esters with high enantioselectivity. We further developed a complementary photochemical protocol that exhibited orthogonal functional-group tolerance toward nitriles and sterically demanding α-naphthyl substituents. Notably, the otherwise counterintuitive change of enantioselectivity at lower temperature can be rationalized by a competing achiral multimolecular proton-shuttle pathway mediated by hydrogen-bonded aniline assemblies. Collectively, these findings could provide a compelling foundation for establishing cooperative catalysis as a key design principle for controlling selectivity in asymmetric carbene chemistry.

Methods

Representative procedure for the Ru-catalyzed asymmetric N–H insertion reaction. A pre-dried 30-mL pear-shaped flask was charged with $[Ru(p\text{-cymene})Cl_2]_2$ (2.4 mg, 0.004 mmol), chiral catalyst (**7**, 2.8 mg, 0.01 mmol), and 4-bromoaniline (**1a**, 103.2 mg, 0.6 mmol). After adding CH_2Cl_2 (3 mL), the mixture was stirred at room temperature under an argon atmosphere for 5 min. A solution of 2-phenylpropan-2-yl 2-diazo-2-phenylacetate (**2a**, 56.0 mg, 0.2 mmol) in CH_2Cl_2 (7 mL) was then added in one portion. The resulting mixture was stirred at room temperature for 12 h. The solvent was removed under reduced pressure, and the crude residue was purified by flash column chromatography on silica gel (*n*-hexane/EtOAc = 15:1) to afford **3a** as a white solid (80.6 mg, 95% yield, 97:3 e.r.).

Representative procedure for the visible-light-promoted asymmetric N–H insertion reaction. A 50-mL Schlenk tube was charged with 4-bromoaniline (**1a**, 206.4 mg, 1.2 mmol), 2-phenylpropan-2-yl 2-diazo-2-(naphthalen-2-yl)acetate (66.1 mg, 0.2 mmol), chiral catalyst (**7**, 1.1 mg, 0.004 mmol), and toluene (10.0 mL). The reaction mixture was irradiated with 450 nm light from a 5 W LED at 4 °C for 12 h. The solvent was removed under reduced pressure, and the crude residue was purified by flash column chromatography on silica gel (*n*-hexane/EtOAc = 15:1) to afford **3p** as a white solid (65.4 mg, 69% yield, 94:6 e.r.).

Data availability

Experimental procedures and characterization data for the synthesized compounds are included in the Supplementary Information. Crystallographic data have been deposited with the Cambridge Crystallographic Data Centre under the following accession number: **3x** (CCDC 2556663). All other data supporting the findings of this study are available from the corresponding authors upon reasonable request.

References

1. Wang, J., Che, C.-M. & Doyle, M. P. *Transition Metal-Catalyzed Carbene Transformations* (Wiley-VCH, 2022, ISBN: 978-3-527-82915-6.).
2. Zhang, F., Wen, H. & Jiang, Y. Transition-metal catalyzed carbene transformations via ring strain-release processes. *ACS Catal.* **16**, 3013–3071 (2026).
3. Davies, H. M. L., Du Bois, J. & Yu, J.-Q. C–H functionalization in organic synthesis. *Chem. Soc. Rev.* **40**, 1855–1856 (2011).
4. Inagaki, T., Kodama, T. & Tobisu, M. Catalytic synthesis of β-lactam derivatives by carbonylative cycloaddition of acylsilanes with imines via a palladium Fischer-carbene intermediate. *Nat. Catal.* **7**, 132–138 (2024).
5. Ogawa, H., Yu, L., Li, S., Nagata, Y., Chan, T. K., Matsuda, Y., Liu, J., Li, Y.-X. & Nakamura, H. Reprogramming RiPP scaffolds through skeletal editing unlocks chemical space. *ChemRxiv* (2026).
6. Sun, Q., Belting, J.-N., Hauda, J., Tymann, D., Antoni, P. W., Goddard, R. & Hansmann, M. M. Spiro-C(sp^3)-atom transfer: Creating rigid three-dimensional structures with Ph_2SCN_2. *Science* **387**, 885–892 (2025).
7. Hutskalova, V. & Sparr, C. Aromatic ring-opening metathesis. *Nature* **638**, 697–703 (2025).
8. Zhu, C., Das, S., Guin, A., De, C. K. & List, B. Organocatalytic regio- and stereoselective cyclopropanation of olefins. *Nat. Catal.* **8**, 487–494 (2025).
9. Zhang, Z. & Gevorgyan, V. Visible light-induced reactions of diazo compounds and their precursors. *Chem. Rev.* **124**, 7214–7261 (2024).
10. Caballero, A., Despagnet-Ayoub, E., Díaz-Requejo, M. M., Díaz-Rodríguez, A., González-Núñez, M. E., Mello, R., Muñoz, B. K., Ojo, W.-S., Asensio, G., Etienne, M. & Pérez, P. J. Silver-catalyzed C–C bond formation between methane and ethyl diazoacetate in supercritical CO_2. *Science* **332**, 835–838 (2011).
11. Goto, Y., Sano, M., Sumida, Y. & Ohmiya, H. N-heterocyclic carbene- and organic photoredox-catalysed meta-selective acylation of electron-rich arenes. *Nat. Synth.* **2**, 1037–1045 (2023).
12. Zheng, Y.-X., Liu, L.-G., Hu, T.-Q., Li, X., Xu, Z., Hong, X., Lu, X., Zhou, B. & Ye, L.-W. Asymmetric Büchner reaction and arene cyclopropanation via copper-catalyzed controllable cyclization of diynes. *Nat. Commun.* **15**, 9227 (2024).
13. Huang, M.-Y. & Zhu, S.-F. Uncommon carbene insertion reactions. *Chem. Sci.* **12**, 15790–15801 (2021).
14. Liao, K., Pickel, T. C., Boyarskikh, V., Bacsa, J., Musaev, D. G. & Davies, H. M. L. Site-selective and stereoselective functionalization of non-activated tertiary C–H bonds. *Nature* **551**, 609–613 (2017).
15. Gu, X., Mo, X., Bai, W.-J., Xie, P., Hu, W. & Jiang, J. Catalytic asymmetric P–H insertion reactions. *J. Am. Chem. Soc.* **145**, 20031–20040 (2023).
16. Nguyen, K. N. M., Mo, X., DeMuynck, B. M., Elsayed, M., Garwood, J. J. A., Ngo, D. T., Rana, I. K. & Nagib, D. A. Harnessing carbene polarity: Unified catalytic access to donor, neutral, and acceptor carbenes. *Science* **389**, 183–189 (2025).
17. Zhao, J., Ji, S., Guo, C., Li, H., Dong, J., Guo, P., Wang, D., Li, Y. & Toste, F. D. A heterogeneous iridium single-atom-site catalyst for highly regioselective carbenoid O–H bond insertion. *Nat. Catal.* **4**, 523–531 (2021).
18. Liu, Z., Yang, Y., Song, Q., Li, L., Zanoni, G., Liu, S., Xiang, M.,

Anderson, E. A. & Bi, X. Chemoselective carbene insertion into the N–H bonds of $NH_3 \cdot H_2O$. *Nat. Commun.* **13**, 7649 (2022).
19. Gillingham, D. & Fei, N. Catalytic X–H insertion reactions based on carbenoids. *Chem. Soc. Rev.* **42**, 4918–4931 (2013).
20. Li, M.-L., Yu, J.-H., Li, Y.-H., Zhu, S.-F. & Zhou, Q.-L. Highly enantioselective carbene insertion into N–H bonds of aliphatic amines. *Science* **366**, 990–994 (2019).
21. Zhang, X.-G., Yang, Z.-C., Pan, J.-B., Liu, X.-H. & Zhou, Q.-L. Enantioselective synthesis of chiral amides by carbene insertion into amide N–H bond. *Nat. Commun.* **15**, 4793 (2024).
22. Zhang, X.-G., Chen, J., Ye, M., Liu, X.-H. & Zhou, Q.-L. Chiral isourea-catalyzed enantioselective carbene insertion into an N–H bond through a double proton-transfer process. *J. Am. Chem. Soc.* **148**, 13513–13519 (2026).
23. Nam, D., Tinoco, A., Shen, Z., Adukure, R. D., Sreenilayam, G., Khare, S. D. & Fasan, R. Enantioselective synthesis of α-trifluoromethyl amines via biocatalytic N–H bond insertion with acceptor–acceptor carbene donors. *J. Am. Chem. Soc.* **144**, 2590–2602 (2022).
24. Furniel, L. G., Echemendía, R. & Burtoloso, A. C. B. Cooperative copper-squaramide catalysis for the enantioselective N–H insertion reaction with sulfoxonium ylides. *Chem. Sci.* **12**, 7453–7459 (2021).
25. Pan, J.-B., Zhang, X.-G., Shi, Y.-F., Han, A.-C., Chen, Y.-J., Ouyang, J., Li, M.-L. & Zhou, Q.-L. A spiro phosphamide catalyzed enantioselective proton transfer of ylides in a free carbene insertion into N–H bonds. *Angew. Chem. Int. Ed.* **62**, e202300691 (2023).
26. Lee, E. C. & Fu, G. C. Copper-catalyzed asymmetric N–H insertion reactions: couplings of diazo compounds with carbamates to generate α-amino acids. *J. Am. Chem. Soc.* **129**, 12066–12067 (2007).
27. Xu, X., Zavalij, P. Y. & Doyle, M. P. Synthesis of tetrahydropyridazines by a metal–carbene-directed enantioselective vinylogous N–H insertion/Lewis acid-catalyzed diastereoselective Mannich addition. *Angew. Chem. Int. Ed.* **51**, 9829–9833 (2012).
28. Arredondo, V., Hiew, S. C., Gutman, E. S., Premachandra, I. D. U. A. & Van Vranken, D. L. Enantioselective palladium-catalyzed carbene insertion into the N–H bonds of aromatic heterocycles. *Angew. Chem. Int. Ed.* **56**, 4156–4159 (2017).
29. Yang, J., Ruan, P., Yang, W., Feng, X. & Liu, X. Enantioselective carbene insertion into the N–H bond of benzophenone imine. *Chem. Sci.* **10**, 10305–10309 (2019).
30. Yang, W., Pu, M., Lin, X., Chen, M., Song, Y., Liu, X., Wu, Y.-D. & Feng, X. Enantioselective formal vinylogous N–H insertion of secondary aliphatic amines catalyzed by a high-spin cobalt(II) complex. *J. Am. Chem. Soc.* **143**, 9648–9656 (2021).
31. Liu, Z., Calvó-Tusell, C., Zhou, A. Z., Chen, K., Garcia-Borràs, M. & Arnold, F. H. Dual-function enzyme catalysis for enantioselective carbon–nitrogen bond formation. *Nat. Chem.* **13**, 1166–1172 (2021).
32. Li, M.-L., Pan, J.-B. & Zhou, Q.-L. Enantioselective synthesis of amino acids from ammonia. *Nat. Catal.* **5**, 571–577 (2022).
33. Ito, T., Harada, S., Homma, H., Takenaka, H., Hirose, S. & Nemoto, T. Asymmetric intramolecular dearomatization of nonactivated arenes with ynamides for rapid assembly of fused ring system under silver catalysis. *J. Am. Chem. Soc.* **143**, 604–611 (2021).
34. Harada, S., Takenaka, H., Ito, T., Kanda, H. & Nemoto, T. Valence-isomer selective cycloaddition reaction of cycloheptatrienes-norcaradienes. *Nat. Commun.* **15**, 2309 (2024).
35. Harada, S., Hirose, S., Takamura, M., Furutani, M., Hayashi, Y. & Nemoto, T. Silver(I)/dirhodium(II) catalytic platform for asymmetric N–H insertion reaction of heteroaromatics. *J. Am. Chem. Soc.* **146**, 733–741 (2024).
36. Peacock, H., Fucini, R. V., Jayalath, P., Ibarra-Soza, J. M., Haringsma, H. J., Flanagan, W. M., Willingham, A. & Beal, P. A. Nucleobase and ribose modifications control immunostimulation by a microRNA-122-mimetic RNA. *J. Am. Chem. Soc.* **133**, 9200–9203 (2011).
37. Kafle, P., Herndon, D. & Sharma, I. Sulfenylcarbene-mediated carbon atom insertion for the late-stage functionalization of N-heterocycles. *J. Am. Chem. Soc.* **147**, 13824–13832 (2025).
38. Chen, Y., Zhang, R., Chen, Z., Liao, J., Song, X., Liang, X., Wang, Y., Dong, J., Singh, C. V., Wang, D., Li, Y., Toste, F. D. & Zhao, J. Heterogeneous rhodium single-atom-site catalyst enables chemoselective carbene N–H bond insertion. *J. Am. Chem. Soc.* **146**, 10847–10856 (2024).
39. Zhang, R., Sun, M., Lu, L., You, S.-L., Niu, Z. & Zhao, J. Effective coordination promoted carbene N–H bond insertion on heterogeneous Cu catalyst. *Angew. Chem. Int. Ed.* **64**, e202517764 (2025).
40. Peng, Q., Huang, M., Xu, G., Zhu, Y., Shao, Y., Tang, S., Zhang, X. & Sun, J. Asymmetric N-alkylation of 1H-indoles via carbene insertion reaction. *Angew. Chem. Int. Ed.* **62**, e202313091 (2023).
41. Golec, J. C., Tan, D.-H., Yamazaki, K., Tiekink, E. H., Christensen, K. E., Hamlin, T. A. & Dixon, D. J. Catalytic enantioselective synthesis of alkylidenecyclopropanes. Nature 645, 932–938 (2025).
42. Krautwald, S., Sarlah, D., Schafroth, M. A. & Carreira, E. M. Enantio- and diastereodivergent dual catalysis: α-allylation of branched aldehydes. *Science* **340**, 1065–1068 (2013).
43. Ovian, J. M., Vojáčková, P. & Jacobsen, E. N. Enantioselective transition-metal catalysis via an anion-binding approach. *Nature* **616**, 84–89 (2023).
44. Shibasaki, M., Kanai, M., Matsunaga, S. & Kumagai, N. Recent progress in asymmetric bifunctional catalysis using multimetallic systems. *Acc. Chem. Res.* **42**, 1117–1127 (2009).
45. Maas, G. Ruthenium-catalysed carbenoid cyclopropanation reactions with diazo compounds. *Chem. Soc. Rev.* **33**, 183–190 (2004).
46. Miyazawa, T., Suzuki, T., Kumagai, Y., Takizawa, K., Kikuchi, T., Kato, S., Onoda, A., Hayashi, T., Kamei, Y., Kamiyama, F., Anada, M., Kojima, M., Yoshino, T. & Matsunaga, S. Chiral paddle-wheel diruthenium complexes for asymmetric catalysis. *Nat. Catal.* **3**, 851–858 (2020).
47. Empel, C., Pei, C. & Koenigs, R. M. Unlocking novel reaction pathways of diazoalkanes with visible light. *Chem. Commun.* **58**, 2788–2798 (2022).
48. Ren, Y.-Y., Zhu, S.-F. & Zhou, Q.-L. Chiral proton-transfer shuttle catalysts for carbene insertion reactions. *Org. Biomol. Chem.* **16**, 3087–3094 (2018).
49. Inoue, Y., Yokoyama, T., Yamasaki, N. & Tai, A. An optical yield that increases with temperature in a photochemically induced enantiomeric isomerization. *Nature* **341**, 225–226 (1989).
50. Peeters, M., Baldinelli, L., Leutzsch, M., Caló, F., Auer, A. A., Bistoni, G. & Fürstner, A. In situ observation of elusive dirhodium carbenes and studies on the innate role of carboxamidate ligands in dirhodium paddlewheel complexes: a combined experimental and computational approach. *J. Am. Chem. Soc.* **146**, 26466–26477 (2024).
51. Elkin, M. & Newhouse, T. R. Computational chemistry strategies in natural product synthesis. *Chem. Soc. Rev.* **47**, 7830–7844 (2018).
52. Nakamura, E., Yoshikai, N. & Yamanaka, M. Mechanism of C–H bond activation/C–C bond formation reaction between diazo compound and alkane catalyzed by dirhodium tetracarboxylate. *J. Am. Chem. Soc.* **124**, 7181–7192 (2002).
53. Falivene, L., Cao, Z., Petta, A., Serra, L., Poater, A., Oliva, R., Scarano, V. & Cavallo, L. Towards the online computer-aided

design of catalytic pockets. *Nat. Chem.* **11**, 872–879 (2019).
54. Bickelhaupt, F. M. & Houk, K. N. Analyzing reaction rates with the distortion/interaction–activation strain model. *Angew. Chem. Int. Ed.* **56**, 10070–10086 (2017).
55. Huo, H., Shen, X., Wang, C., Zhang, L., Röse, P., Chen, L.-A., Harms, K., Marsch, M., Hilt, G. & Meggers, E. Asymmetric photoredox transition-metal catalysis activated by visible light. *Nature* **515**, 100–103 (2014).
56. Ullrich, C. A. A snapshot of time-dependent density-functional theory. *APL Comput. Phys.* **1**, 020901 (2025).
57. Marcus, R. A. Electron transfer reactions in chemistry: theory and experiment. *Angew. Chem. Int. Ed. Engl.* **32**, 1111–1121 (1993).

Acknowledgements
This work was supported in part by JSPS KAKENHI grant numbers JP26K02134, JP25K01760, and JP25H02003 in Transformative Research Areas (A) JP24A202 Integrated Science of Synthesis by Chemical Structure Reprogramming (SReP). It was also partly supported by Digitalization-driven Transformative Organic Synthesis (Digi-TOS, JP24H01059).

Author contributions
S.H. conceived the project. S.H. and T.N. supervised the research. M.F. and T.S. performed the experiments. S.H. and M.F. performed the computational studies. S.H. wrote the manuscript with contributions from all authors. All authors contributed to the preparation and editing of the Supplementary Information. All authors reviewed and approved the final manuscript. We thank Dr. Tomohiro Yazawa (Chiba University) for assistance regarding X-ray crystallographic analysis.

Competing interests
The authors declare no competing interests.

Additional information
Supplementary information The online version contains supplementary material available at https://doi.org/
Correspondence and requests for materials should be addressed to Shingo Harada.

Supplementary Files

This is a list of supplementary files associated with this preprint. Click to download.

- 260618Supplementary.pdf
- CrystalStructure3x.cif
- checkcif3x.pdf